18TH WORLD CONFERENCE ON EARTHQUAKE ENGINEERING
WCEE2024
MILAN

MILAN, ITALY
30TH JUNE - 5TH JULY 2024
www.wcee2024.it

DAMAGE STATE-DEPENDENT FRAGILITY MODELS FOR RC BUILDINGS EXPOSED TO FLOOD AND SEISMIC HAZARDS

P. Gehl[1], K. Trevlopoulos[1] & C. Negulescu[1]

[1] BRGM, Orléans, France, p.gehl@brgm.fr

Abstract: *The exposure of built areas to multiple hazard types, which might be heightened due to external factors such as climate change, requires the development of consistent approaches for the multi-risk assessment of structures throughout their lifetime. To this end, this study focuses on the derivation of damage state-dependent fragility models, for pre-code or low-code reinforced concrete structures representative of buildings found in French city centres. The considered external hazards are among the ones most often encountered in Southern France (e.g., Nice area), i.e. earthquakes (including mainshock-aftershock sequences) and flooding. Fragility models are built via Monte Carlo simulations, where the order of the sequential loadings, as well as their intensity is randomized to generate all possible outcomes and hazard combinations. Using a harmonized damage scale, the result consists of state-based fragility models that provide probabilities of transitioning from all damage states to all higher damage states, given the intensity of one of the two hazard types considered.*

1. Introduction

Accurate multi-hazard risk assessment implies the integration of multi-hazard interactions at the impact or consequence level (e.g., Marzocchi et al., 2012; Selva, 2013; Gehl, 2017), which makes the development of multi-hazard fragility models necessary. In recent years, a growing number of research studies have proposed multi-hazard frameworks that strive to account for the wide range of possible interactions between multiple hazard types. Gill & Malamud (2014) have worked on an extensive identification of multi-hazard interactions, by distinguishing between hazards that trigger each other, hazards that alter the probability of occurrence of another hazard, and hazards with spatial and temporal coincidence. Bruneau et al. (2017) have adopted a similar classification, while considering also hazards that interact through impacts on physical components. Alternatively, in their review of social vulnerability studies in a multi-hazard context, Drakes & Tate (2022) have adopted a multi-hazard classification that covers aggregate hazards, cascading hazards and compound hazards.

De Angeli et al. (2022) developed a multi-hazard framework for spatial-temporal impact analysis, which they applied to a scenario in the Po valley including an earthquake followed by a flood. They inventoried all possible interaction mechanisms between multiple hazards in six categories: parallel hazards, cascading hazards, disposition alteration, additional hazard potential, coincident triggering, and cyclic triggering. In the case of sequential actions of hazards overlapping in space, they underlined the challenge of quantifying the effect of the residual damage on the impacts of following hazards.

According to the review by Gentile et al. (2022) of physical impact models for multi-hazard risk assessment, the classification proposed by Zaghi et al. (2016) is adapted to study of multi-hazard fragility models, since it relies on two types of interactions:

- Level-I Interactions, representing natural interactions of hazards independent of the presence of physical components;
- Level-II Interactions, representing interactions through the effects of hazards on a given site, component or infrastructure.

The latter type of interactions is of most interest here, since it focuses on the impact on physical components, whatever the type or origin of the multiple hazard combinations (e.g., concurrent, successive, triggered, independent, etc.). What matters is the alteration of the physical or functional properties of an asset (e.g., fragility/vulnerability curve) due to cumulative damage. For this reason, multi-hazard fragility also includes repeated instances of the same hazard, such as earthquake sequences or compound flooding (Gentile et al., 2022).

However, the development of multi-hazard models remains relatively limited, with respect to the wide range of possible multi-hazard combinations and the variety of exposed assets to consider. This technical gap may be explained by several factors, such as differences in the scientific maturity between the various hazard assessment fields (Douglas, 2007), the need to integrate different physical phenomena in the structural modelling step, and the lack of harmonised damage scales between various hazard loading mechanisms.

The assessment of cumulative damage also requires state-dependent fragility curves, i.e. fragility curves conditioned on the damage state of the element in addition to the hazard intensity measure. Gómez Zapata et al. (2023) developed a procedure for converting typical single-hazard fragility curves to state-dependent fragility curves to account for cumulative damage. This procedure has been developed as an alternative to the development of new synthetic or empirical state-dependent fragility curves. They applied this procedure in scenario-based multi-risk assessment in the case of an earthquake in Lima (Peru) followed by a tsunami. To overcome the difficulties due to the differences between damage scales for different hazards, they introduced "inter-scheme compatibility matrices", which account probabilistically for the correspondences between damage scales.

Therefore, the present study focuses on the derivation of damage state-dependent fragility curves for reinforced-concrete (RC) buildings that are representative of the housing stock in the city of Nice (France). To this end, high-fidelity structural models, designed according to low or moderate code acceleration levels, are subjected to sequences of earthquake and flood loadings in order to estimate state-dependent fragility curves after a statistical treatment. Finally, it is proposed to investigate the effect of various modelling assumptions on the evolution of vulnerability due to cumulated loadings.

2. Modelling framework

2.1. General principle

State-dependent fragility curves are numerically derived by subjecting structural models of a RC building to a chain of successive loadings. In the simulations, the models are subjected to loading time-histories which include four steps, as schematized in Figure 1.

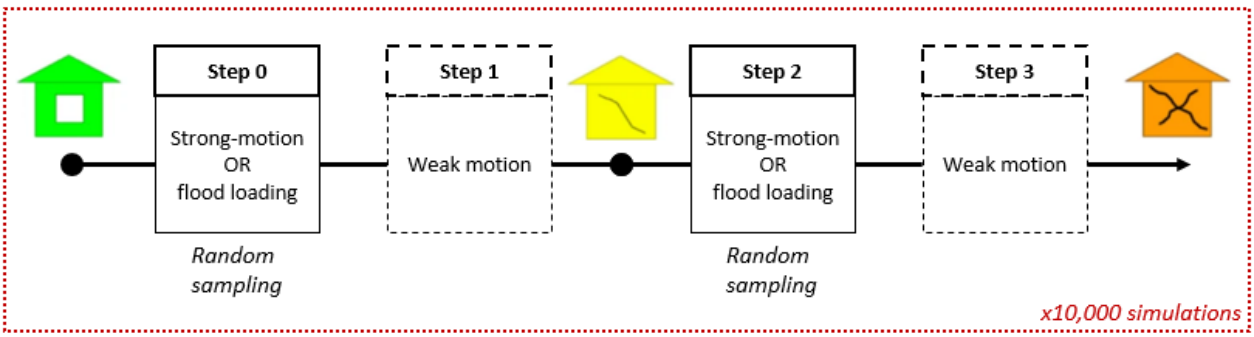

Figure 1. Adopted schema for the derivation of state-dependent fragility curves.

During the first and the third step (or Steps 0 and 2, respectively), the potentially damaging hazard loads are applied to the building models. The type of hazard loads may be a strong ground motion or flood loads, and the type of loads is randomly chosen for Steps 0 and 2 in each simulation. During the second and fourth step (Steps 1 and 3), a weak ground motion of a very low intensity (PGA < 10^{-3} g) is applied at the base of the building model. Steps 1 and 3 allow the dissipation of any strong vibration of the building model in Steps 0 and 2, while the weak ground motion may assist the identification of the dynamic characteristics of the building model as well as its damage state.

2.2. Structural modelling

The approach is applied to existing RC buildings in the city center of Nice (France), which is exposed to an average seismicity level (i.e. the highest level in mainland France) according to the French seismic zonation (). This area is also at risk of recurring floods near the Var and Paillon rivers. The distribution of the building stock has been obtained from the exposure model (Crowley et al., 2021a) of the European Seismic Risk Model 2020 (ESRM20, Crowley et al., 2021b). Using simplified classes of the GEM taxonomy (Brzev et al., 2013), the distribution of RC buildings in Nice is detailed in Table 1.

Table 1. Simplified distribution of RC building types in Nice municipality, according to the ESRM20 exposure model (Crowley et al., 2021a).

Macro Taxonomy	Class	Percentage of total number of buildings	Percentage of number of RC buildings
Concrete frame with infill panels, low rise, low/moderate code	CR_LFINF_CDM_HEX_2	9.8	30.3
Concrete frame with infill panels, mid rise, pre code	CR_LFINF_CDL_HEX_4	6.0	18.6
Concrete frame, mid rise, low/moderate code	CR_LFINF_DUM_HEX_4	0.1	0.2
Concrete frame, mid rise, pre code	CR_LFM_CDL_HEX_4	1.5	4.8
Concrete wall, low rise, pre code	CR_LWAL_DUL_HEX_2	1.0	3.0
Concrete wall, mid rise, low/moderate code	CR_LWAL_DUM_HEX_4	2.4	7.5
Concrete wall, mid rise, pre code	CR_LWAL_DUL_HEX_4	11.6	35.6

The response of the building models to the earthquake and flood loads is modeled using OpenSeesPy (Zhu et al., 2018). All building models are two-dimensional. Although simplified 2D archetype models are unable to account for effects related to irregularities such as torsion, it has been shown that they can be used to make an effective estimation of losses of real 3D structures (Kappos et al., 2006). Three type of analysis are used: fiber, modal and non-linear time-history analyses. The fiber analyses are employed to calibrate bilinear moment-curvature hysteretic models, which are used in the context of distributed plasticity modelling. Pinching in the moment-curvature loops is used only for the structural walls with a factor of 0.3 assuming a strong pinching effect. In the fiber analyses, reinforcement steel is modeled using the Steel02 material in OpenSeesPy. The strength degradation of confined concrete is modeled using the material Concrete02 in OpenSeesPy. The infill walls are modeled with double struts as in Karapetrou et al. (2016) with a compressive strength of 3.2 MPa and an elastic modulus of 3.2 GPa. The inelastic behavior of the struts is modeled using the hysteretic material in OpenSees. Modal analyses are used to compute the fundamental period of the models in their undamaged states. In the total mass of each model, the mass corresponding to structural elements, infill walls, live and dead loads of the slab floors are included. Since a hysteretic law with stiffness degradation is used for bending behavior in the dynamic analyses, which models stiffness degradation after yield, the stiffness of the elements is taken into account equal to a fraction of the un-cracked stiffness, which fits the moment-curvature results of the fiber analysis. The simulations consider P-Delta effects caused by second-order moments, fully fixed base nodes, and floors as rigid diaphragms.

Models from the building class CR_LFINF_CDM_11_HEX_2 are taken as an example for the remainder of the study, due to its significant part in the distribution of existing RC buildings (see Table 1). The design of the building model is done based on the taxonomy string, i.e., using modern limit state design, for lateral resistance for seismic loads with a coefficient of 0.11, and without capacity design.

The corresponding capacity curve is shown in Figure 2 Left, along with two capacity curves extracted from the ESRM20 vulnerability model (Romao et al., 2021), for similar building classes (i.e., CR_LINF_CDL_10_H2 and CR_LINF_CDM_10_H2). The modelled capacity curve presents lower initial stiffness, however it has a

higher yielding point. Approximately 20% of the yield spectral acceleration is due to the presence of the infill walls. The ultimate displacement is selected so that the available ductility is equal to 2.25, which is proposed by HAZUS (FEMA 2020) for low rise reinforced concrete buildings with infills.

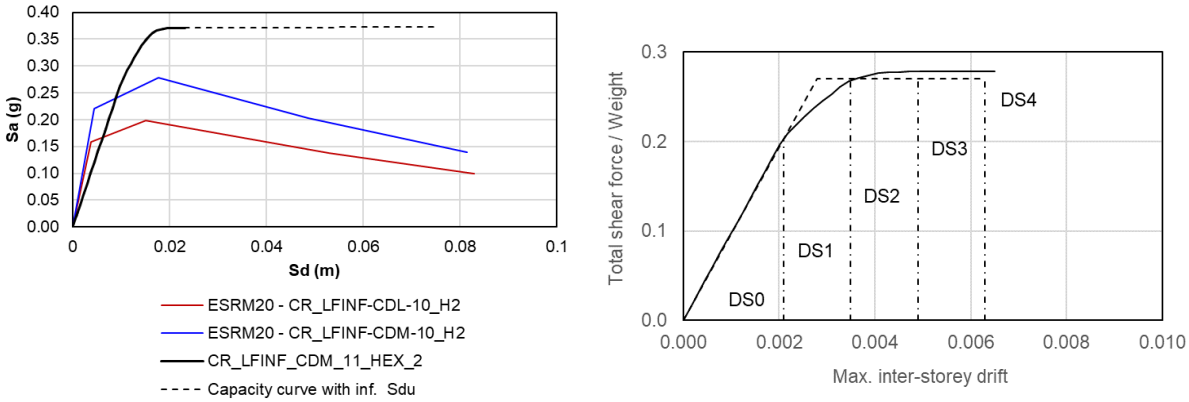

Figure 2. Left: Capacity curve for the CR_LFINF_CDM_11_HEX_2 class building model; Right: Definition of damage states.

We define the thresholds of the damage states by adapting the procedure by Martins and Silva (2021). Their procedure uses the pushover capacity curve in terms of spectral displacement and spectral acceleration to define the damage state thresholds in terms of spectral displacement. An ultimate ductility ratio $d_u / d_y = 2.25$ is chosen as a reasonable assumption. Here, we are using the maximum inter-storey drift (θ) as the Engineering Demand Parameter (EDP); therefore, we use the pushover capacity curve in terms of θ and total shear force-to-weight ratio (see Figure 2 Right). The parametric definition of the damage state thresholds used in this study is given in Table 2.

Table 2. Parametric definition of the damage state thresholds used in this study, from Martins & Silva (2021).

Damage state description	Threshold
DS0: no structural damage (implied)	-
DS1: slight structural damage	$d = 0.75d_y$
DS2: moderate structural damage	$d = 0.50d_y + 0.33d_u$
DS3: extensive structural damage	$d = 0.25d_y + 0.67d_u$
DS4: complete structural damage	$d = d_u$

Finally, four variants of the CR_LFINF_CDM_11_HEX_2 model are considered, depending on various assumptions of the hysteretic behavior during cyclic loadings. The objective is to investigate the effects of these modelling assumptions on the evolution of the state-dependent fragility curves. The description of the four models in detailed in Table 4.

Table 3. Definition of the four models with respect to their hysteretic material parameters, as defined in OpenSees. The parameter "pinchY" is the pinching factor for stress during reloading (value of 1.0 implies no pinching). The parameter "damage1" is the damage factor due to ductility (value of 0.0 implies no strength degradation). The parameter "damage2" is the damage factor due to energy (value of 0.0 implies no strength degradation).

Model	*pinchY*	*damage1*	*damage2*	Description
1	1.0	0.0	0.0	no pinching; no strength degradation
2	0.5	0.0	0.0	pinching; no strength degradation
3	0.5	0.1	0.0	pinching; strength degradation related to damage due to ductility only
4	0.5	0.1	0.1	pinching; strength degradation related to damage due to both ductility and in-cycle energy dissipation

2.3. Applied external loadings

The strong ground motion is applied as a time-history of displacements of the nodes at the base of the building model. The time-history of a ground motion is randomly selected among the horizontal components of 294 three-dimensional records selected from the Engineering Strong Motion Database (Luzi et al., 2016; Lanzano et al., 2022) for a minimum earthquake magnitude of 6.0, a maximum epicentral distance of 30 km, and a PGA of 1 cm/s^2 (≈ 10^{-3} g).

The flood loads are horizontal loads applied to the exterior columns on one side of the building models, and include the hydrostatic pressure, and the hydrodynamic pressure. Based on Baiguera et al. (2022), the hydrodynamic stress is assumed to have a uniform distribution along the inundation depth, while total flood loads (Eq. 1) are discretized and applied as 5 forces over the length of each column.

$$F = \frac{1}{2}\rho \cdot C_d \cdot C_{cx} \cdot B \cdot (h \cdot u^2) \quad (1)$$

Where ρ is the density of water, C_d is the drag coefficient, C_{cx} = 0.7 the proportion closure coefficient, B is the building width in the direction perpendicular to the flow, h the inundation depth, and u the flow velocity.

3. Multi-hazard fragility assessment

3.1. Seismic fragility of the intact model

The simulation scheme presented in Section 2.1 is applied, with 10,000 stochastic realizations of the Step 0 – Step 3 loading chains. In order to evaluate the seismic fragility of the model in its intact state (i.e., without any prior loadings), the outcomes of the simulations right after Step 0 are taken, and only if the Step 0 simulations consist of seismic time-history loadings. With this dataset, fragility curves for the four damage states are derived, using PGA as Intensity Measure (IM). Fragility parameters are estimated with an ordinal Generalized Linear Modelling (GLM) procedure, using probit (ϕ^{-1}) as the link function. As a result, the functional form of a fragility curve, expressing the probability of exceeding a damage state DS_i given PGA, is defined as follows:

$$P(ds \geq DS_i | PGA) = \Phi\left(\frac{\ln PGA - \ln \alpha_i}{\beta}\right) \quad (2)$$

where α_i and β are the fragility parameters (median and standard deviation) and ϕ is the standard normal cumulative distribution function. The ordinal regression applied here prevents successive fragility curves from crossing each other, since it forces a unique standard deviation for all four damage states. Results are presented in Table 4, and they are compared with the fragility parameters provided by ESRM20 for the two similar building classes.

Table 4. Fragility parameters for the intact CR_LFINF_CDM_11_HEX_2 models, along with the fragility values provided for the two corresponding ESRM20 models.

Model	α_{DS1}	α_{DS2}	α_{DS3}	α_{DS4}	β
CR_LFINF_CDM_11_HEX_2 – Model 1	0.240	0.356	0.451	0.541	0.29
CR_LFINF_CDM_11_HEX_2 – Model 2	0.233	0.332	0.414	0.516	0.32
CR_LFINF_CDM_11_HEX_2 – Model 3	0.182	0.257	0.333	0.390	0.42
CR_LFINF_CDM_11_HEX_2 – Model 4	0.182	0.257	0.333	0.390	0.42
CR_LINF-CDL-10_H2 (ESRM20)	0.354	0.491	0.639	0.781	1.21
CR_LINF-CDM-10_H2 (ESRM20)	0.403	0.569	0.745	0.912	1.10

The two ESRM20 models have higher fragility medians than the CR_LFINF_CDM_11_HEX_2 models, which may be explained by the fact that they have a larger ultimate displacement. Moreover, they also have much larger standard deviations: in our simulations, only record-the-record variability is accounted for; adding other components of variability, such as modelling assumptions, intra-class building variability or damage threshold definition, would result in more comparable β values.

When comparing the four CR_LFINF_CDM_11_HEX_2 models which each other, it appears that pinching and especially strength degradation result in lower fragility medians than Model 1, which only accounts for stiffness degradation. Model 3 and 4 have the same fragility parameters because the dynamic analyses have yielded

almost identical EDP values, which results in negligible difference when performing the ordinal GLM regression. This observation shows that the parameter "damage2" for strength degradation (see Table 3) has little influence on the simulation outcomes, at least in the case of an intact model.

3.2. State-dependent seismic fragility

A similar procedure is applied when deriving state-dependent fragility curves: in this case, outcomes of Step 2 are examined, only for Step 2 simulations consisting of seismic time-history loadings. Outcomes of Step 0 are used to determine the initial state of the model. Since the initial state of the model may be incurred by either seismic or flood loadings (i.e., depending on what type of simulation was randomly selected during Step 0), it is necessary to check whether the type of prior loading influences the state-dependent fragility curves or if the knowledge of the initial state is a sufficient condition. In the latter case, such state-dependent fragility curves would satisfy the Markov assumption and would constitute a powerful tool to assess the evolution of structural vulnerability throughout the lifetime of the studied building.

The parameters of the state-dependent fragility curves, $P(ds \geq DS_i \mid PGA, DS_{j,all})$, with DS_i representing the damage state to exceed in the current step and $DS_{j,all}$ the initial damage state whatever the type of prior loading, are estimated using ordinal GLM regression and they are detailed in Table 5, using Model 3 as an example. Corresponding fragility curves for are plotted in Figure 3.

Table 5. State-dependent fragility parameters for Model 3.

Initial state $DS_{j,all}$	α_{DS1}	α_{DS2}	α_{DS3}	α_{DS4}	β
DS0	0.182	0.257	0.333	0.390	0.42
DS1	-	0.205	0.258	0.301	0.45
DS2	-	-	0.201	0.257	0.67
DS3	-	-	-	0.034	1.02

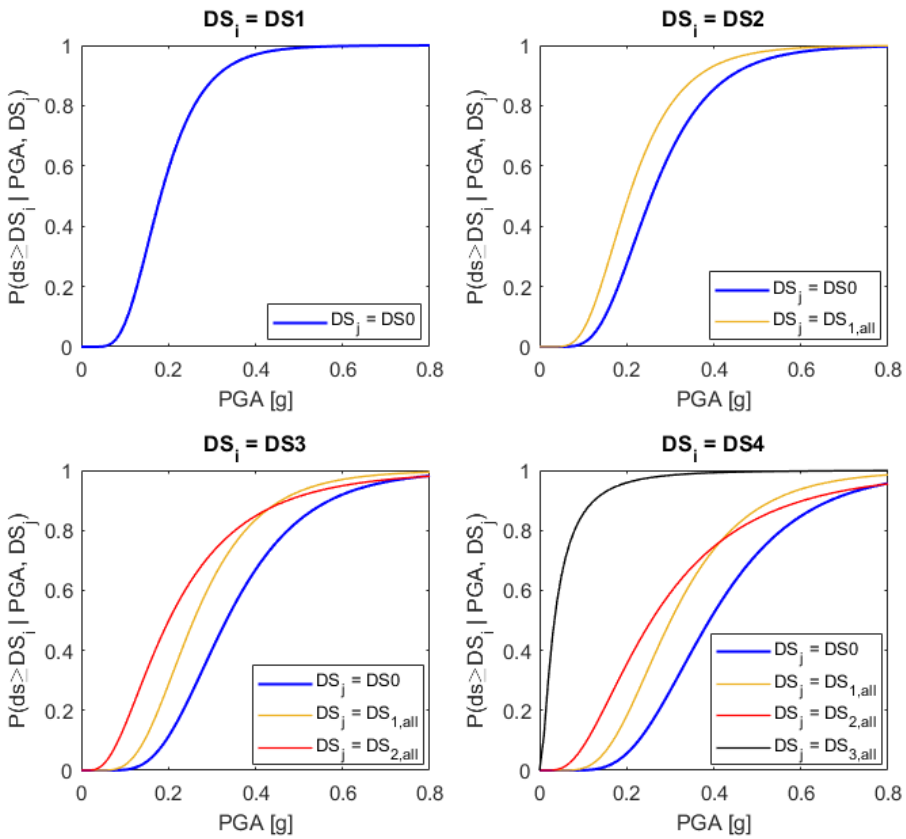

Figure 3. State-dependent seismic fragility curves for Model 3. The fragility curves for the intact model are plotted as blue lines.

As expected, the median fragility parameter decreases as the initial damage state increases. This is especially the case when comparing the fragility parameters between initial DS_j = *DS0* and the rest, and also between DSj = DS3 and the rest. The differences between initial DS_j = *DS1* and DS_j = *DS2* (orange and red curves in the bottom plots of Figure 3) are much less significant, with even some overlap between the curves at larger intensities. This may be due to the proximity between *DS1* and *DS2* in terms of ductility; both damage states being close to the yielding point of the capacity curve (see Figure 2).

There is also a sharp increase of the standard deviation parameter β, which may explain the overlap between the orange and red curves. For higher initial damage states, an increase in the standard deviation is due to the existence of a larger population of models with possibly different local damage configurations belonging to the same initial state, which creates more variability in the fragility model. However, another reason might be the elongation of the fundamental period of the models as damage states increase, so that PGA might become a less efficient IM.

3.3. Influence of hysteretic modelling assumptions

Similarly to the study of Model 3 in the previous sub-section, state-dependent fragility curves are also derived for the other models (Model 1 to 4, as described in Table 3). In order to compare all models, the evolution of the state-dependent fragility medians, normalized by their respective intact-state values (see Table 4), is plotted as bar diagrams in Figure 4.

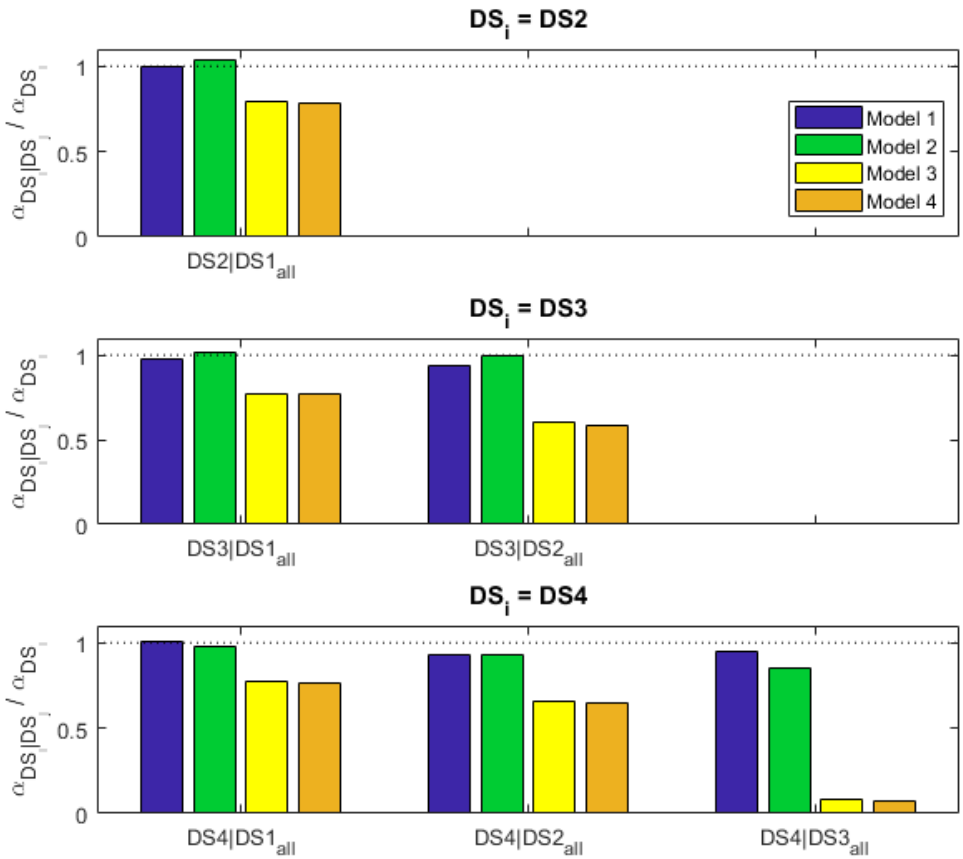

Figure 4. Relative evolution of the fragility median (ratio of state-dependent $\alpha_{DSi|DSj}$ over intact α_{DSi}), for the four model variants.

Values should be below 1 in order to reproduce an increase of the vulnerability of previously damaged structures. Moreover, as the initial damage DS_j increases, the ratio values should decrease (i.e., from left to right in bar plots). Such behavior is indeed observed for Models 3 and 4; it is also found that differences between these two variants are not significant, which means that the the strength degradation due to in-cycle energy dissipation (i.e., hysteretic parameter “damage2” in Table 3) has little influence in the present case.

On the other hand, Models 1 and 2 that are based on stiffness degradation demonstrate similar evolutions, and their median ratios remain very close to 1. As a result, it may be concluded that accounting for strength degradation in the hysteretic behavior is necessary in order to properly model the effects of damage accumulation. Only in the case of damage state $DS_i = DS4$ (i.e., fragility curves for complete damage), it may be observed that the median ratios for Models 1 and 2 drop consistently below 1, although at a much lower rate than the other models. In the bottom plot of Figure 4, the effect of pinching in the hysteretic behavior starts also to become more noticeable.

3.4. Influence of hazard type in the loading history

Similar state-dependent fragility curves are also derived by distinguishing now the type of hazard loading simulated in Step 0. The results are presented in Table 6 and Figure 5, where the fragility parameters are different depending on whether the initial damage state has be induced by an earthquake ($DS_{j,EQ}$) or by a flood ($DS_{j,FL}$). The focus here is on Model 3, since it has been shown in the above discussion that Modes 3 and 4 yield very similar results, and that Models 1 and 2 are not able to properly account for the effects of damage accumulation.

Table 6. State-dependent fragility parameters for CR_LFINF_CDM_11_HEX_2 Model 3, in the cases where the initial state is induced by a seismic loading ($DS_{j,EQ}$) or by a flood loading ($DS_{j,FL}$).

Initial state DS_j	α_{DS1}	α_{DS2}	α_{DS3}	α_{DS4}	β
DS0	0.182	0.257	0.333	0.390	0.42
$DS1_{EQ}$	-	0.203	0.241	0.284	0.49
$DS1_{FL}$	-	0.210	0.311	0.357	0.39
$DS2_{EQ}$	-	-	0.186	0.240	0.67
$DS2_{FL}$	-	-	0.325	0.375	0.42
$DS3_{EQ}$	-	-	-	0.033	1.03
$DS3_{FL}$	-	-	-	0.097	0.94

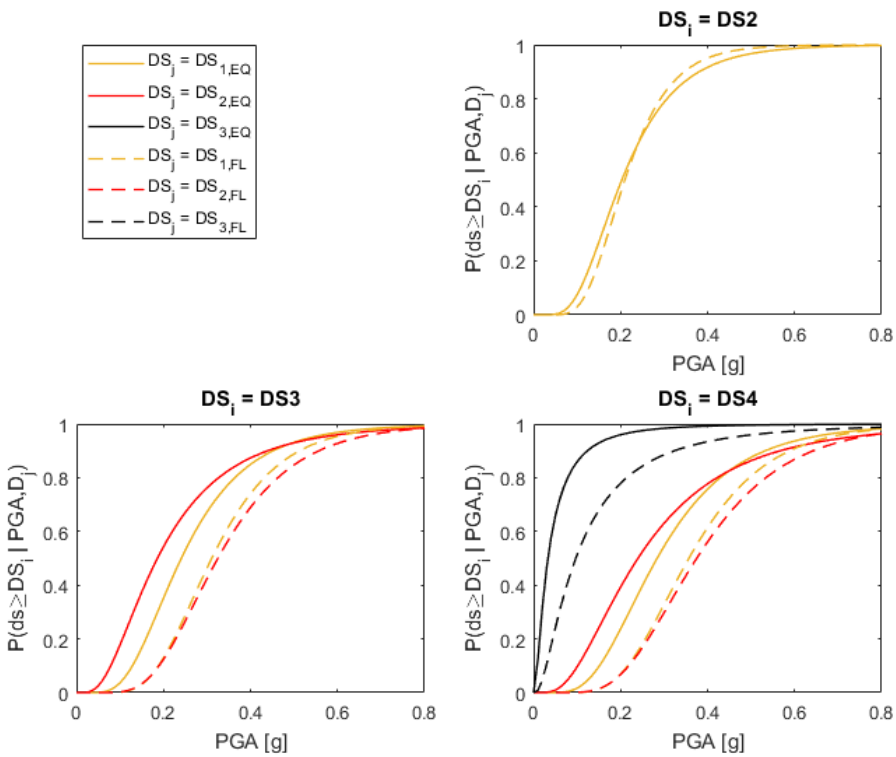

Figure 5. State-dependent seismic fragility curves for Model 3, in the cases where the initial state is induced by a seismic loading (solid lines) or by a flood loading (dashed lines).

Fragility curves for damage states DS_i = *DS2* are very close to each other, showing little difference whether the initial state DS_j = *DS1* has been caused by seismic or flood loading. However, for larger initial states DS_j (i.e., bottom plots of Figure 5), much larger differences start to appear; and the state-dependent fragility curves based on flood loading in the first step do not experience a significant decrease of their median value when the initial state gets larger. There is even an inversion between the fragility curves $P(ds \geq DS_i \mid DS_{1,FL})$ and $P(ds \geq DS_i \mid DS_{2,FL})$.

Possible reasons for this observation include the absence of repeated cycling loadings when apply the flood load in Step 0 (as opposed to the seismic load), as well as the potential differences in the local damage distribution between the two types of loading. The latter point would require further investigations, such as the identification of the locations of the damaged structural elements or the creation of specific mechanisms such as soft-story, etc. Such work would then support the creation of a more precise damage scale, in order to account for the types of damage that may be specific to each loading type.

4. Conclusions

In a context of multi-hazard risk assessment accounting for interactions at the structural level (i.e., damage accumulation from potentially unrelated hazard events), this study has proposed to investigate the numerical derivation of state-dependent fragility curves for RC structures exposed to flood-earthquake or earthquake-earthquake sequences. The RC structure of interest has been designed based on an inventory of the building stock of the city of Nice (France), in order to construct a realistic model of low/moderate code structures.

Various assumptions have been tested regarding the modelling of the hysteretic behavior. Results show that models based on stiffness degradation only are not able to properly account for damage accumulation. The role of pinching is somewhat limited as well, especially for low to moderate damage states. Strength degradation related to damage due to ductility appears to be the most important parameter, while the results do not change much when strength degradation due to in-cycle energy dissipation is also added to the model.

While the initial objective was to develop state-dependent fragility curves that would be independent of the loading history of the structure, current results show that differences between state-dependent curves are too important when the initial damage has been induced by seismic or flood loadings. This finding does not enable the validation of the Markov assumption when applying such state-dependent fragility curves. Further work on the identification of local damage mechanisms and on the refinement of the damage scale (i.e., current based on maximum inter-story drift only) should constitute useful ways of improvement.

5. References

Baiguera M., Rossetto T., Robertson I.N., Petrone C. (2022). A Procedure for Performing Nonlinear Pushover Analysis for Tsunami Loading to ASCE 7, *Journal of Structural Engineering*, 148:04021270.

Bruneau M., Barbato M., Padgett J.E., Zaghi A.E., Mitrani-Reiser J., Li Y. (2017). State of the art of multihazard design, *Journal of Structural Engineering*, 143(10): 03117002.

Brzev S., Scawthorn C., Charleson A.W., Allen L., Greene M., Jaiswal K., Silva V. (2013). *GEM Building Taxonomy (Version 2.0)*, GEM Technical Report 2013-02.

Crowley H., Despotaki V., Rodrigues D., Silva V., Costa C., Toma-Danila D., Riga E., Karatzetzou A., Fotopoulou S., Sousa L., Ozcebe S., Gamba P., Dabbeek J., Romão X., Pereira N., Castro J.M., Daniell J., Veliu E., Bilgin H., Adam C., Deyanova M., Ademović N., Atalic J., Bessason B., Shendova V., Tiganescu A., Zugic Z., Akkar S., Hancilar U. (2021a). *European Exposure Model Data Repository [Data set]*, Zenodo, http://doi.org/10.5281/zenodo.4062044

Crowley H., Dabbeek J., Despotaki V., Rodrigues D., Martins L., Silva V., Romão X., Pereira N., Weatherill G., Danciu L. (2021b). *European Seismic Risk Model (ESRM20)*, EFEHR Technical Report 002 V1.0.0, https://doi.org/10.7414/EUC-EFEHR-TR002-ESRM20

De Angeli S., Malamud B.D., Rossi L., Taylor F.E., Trasforini E., Rudari R. (2022). A multi-hazard framework for spatial-temporal impact analysis, *International Journal of Disaster Risk Reduction*, 73: 102829.

Douglas J. (2007). Physical vulnerability modelling in natural hazard risk assessment, *Natural Hazards and Earth System Sciences*, 7(2): 283-288.

Drakes O., Tate E. (2022). Social vulnerability in a multi-hazard context: a systematic review, *Environmental Research Letters*, 17(3): 033001.

FEMA (2020). *Hazus Earthquake Model Technical Manual*.

Gehl P. (2017). Bayesian networks for the multi-risk assessment of road infrastructure, *PhD dissertation, University College London*, London, United Kingdom.

Gentile R., Cremen G., Galasso C., Jenkins L.T., Manandhar V., Menteşe E.Y., ... , McCloskey J. (2022). Scoring, selecting, and developing physical impact models for multi-hazard risk assessment, *International Journal of Disaster Risk Reduction*, 82: 103365.

Gill J.C., Malamud B.D. (2014). Reviewing and visualizing the interactions of natural hazards, *Reviews of Geophysics*, 52(4): 680-722.

Gómez-Zapata J.C., Pittore M., Brinckmann N., et al. (2023). Scenario-based multi-risk assessment from existing single-hazard vulnerability models. An application to consecutive earthquakes and tsunamis in Lima, Peru, *Natural Hazards and Earth System Sciences*, 23: 2203-2228.

Kappos A.J., Panagopoulos G., Panagiotopoulos C., Penelis G. (2006). A hybrid method for the vulnerability assessment of R/C and URM buildings, *Bulletin of Earthquake Engineering*, 4: 391-413.

Karapetrou S., Manakou M., Bindi D., et al. (2016). “Time-building specific” seismic vulnerability assessment of a hospital RC building using field monitoring data, *Engineering Structures*, 112: 114-132.

Lanzano G., Luzi L., Cauzzi C., et al. (2021). Accessing European Strong-Motion Data: An Update on ORFEUS Coordinated Services, *Seismological Research Letters*, 92: 1642-1658.

Luzi L., Puglia R., Russo E., et al. (2016). The Engineering Strong-Motion Database: A Platform to Access Pan-European Accelerometric Data, *Seismological Research Letters*, 87: 987-997.

Martins L., Silva V. (2021). Development of a fragility and vulnerability model for global seismic risk analyses, *Bulletin of Earthquake Engineering*, 19(15): 6719-6745.

Marzocchi W., Garcia-Aristizabal A., Gasparini P., Mastellone M.L., Di Ruocco A. (2012). Basic principles of multi-risk assessment: a case study in Italy, *Natural Hazards*, 62: 551-573.

Romão X., Pereira N., Castro J.M., Crowley H., Silva V., Martins L., De Maio F. (2021). *European Building Vulnerability Data Repository*, Zenodo, https://doi.org/10.5281/zenodo.4062410

Selva J. (2013). Long-term multi-risk assessment: statistical treatment of interaction among risks, *Natural Hazards*, 67: 701-722.

Zaghi A.E., Padgett J.E., Bruneau M., Barbato M., Li Y., Mitrani-Reiser J., McBride A. (2016). Establishing common nomenclature, characterizing the problem, and identifying future opportunities in multihazard design, *Journal of Structural Engineering*, 142(12): H2516001.

Zhu M., McKenna F., Scott M.H. (2018). OpenSeesPy: Python library for the OpenSees finite element framework. *SoftwareX*, 7: 6-11.